

---

# COMPUTING THE CUT LOCUS OF A RIEMANNIAN MANIFOLD VIA OPTIMAL TRANSPORT

---

**Enrico Facca**

Univ. Lille, Inria, CNRS, UMR 8524  
Laboratoire Paul Painlevé  
Lille, France  
enrico.facca@inria.fr

**Luca Berti**

CNRS  
Université de Strasbourg,  
Strasbourg, France  
berti@math.unistra.fr

**Francesco Fassò**

Department of Mathematics “Tullio Levi-Civita”  
University of Padova  
Padova, Italy  
fasso@math.unipd.it

**Mario Putti**

Department of Mathematics “Tullio Levi-Civita”  
University of Padova  
Padova, Italy  
putti@math.unipd.it

## ABSTRACT

In this paper, we give a new characterization of the cut locus of a point on a compact Riemannian manifold as the zero set of the optimal transport density solution of the Monge-Kantorovich equations, a PDE formulation of the optimal transport problem with cost equal to the geodesic distance. Combining this result with an optimal transport numerical solver based on the so-called dynamical Monge-Kantorovich approach, we propose a novel framework for the numerical approximation of the cut locus of a point in a manifold. We show the applicability of the proposed method on a few examples settled on 2d-surfaces embedded in  $\mathbb{R}^3$  and discuss advantages and limitations.

**Keywords** Cut locus · Riemannian Geometry · Optimal Transport Problem · Monge-Kantorovich equations · Geodesic Distance

## 1 Introduction

Given a compact Riemannian manifold  $(M, g)$  of dimension  $n$  and a point  $p \in M$ , the cut locus  $C_p$  of  $p$  is, roughly speaking, the set of points where more than one minimizing geodesic starting from  $p$  arrives. For example, the cut locus of a point in a 2-sphere embedded in  $\mathbb{R}^3$  is its anti-podal point.

The cut locus is a fundamental object of Riemannian geometry, e.g., it determines the topology of  $M$  since  $M \setminus C_p$  is diffeomorphic to an  $n$ -disk [1]. Moreover, the cut locus is intimately related to the singular set of the distance function [2] and thus to the points where caustics form. However, the construction of the cut locus of a point on a manifold is rather difficult and cut locus shape is known only in very special cases, for example, for revolution surfaces [3]. For these reasons there is a strong interest in its numerical construction.

The numerical approximation of the cut locus of  $p$  has seen only sparse and diverse attempts in the past. Many approaches are based on the approximation of geodesics and exponential map. For example, [4] approximate the exponential map by means of piecewise polynomial interpolation and follow the geodesics starting from  $p$  until they are no longer minimal. Direct numerical evaluation of geodesics emanating from  $p$  is another approach often proposed. This is the method of choice in [5], who use a direct discretization by finite differences of the Riemannian partial differential equations. In [6] the authors construct geodesics from shortest paths of graphs constructed on point data. All these methods require some sort of smoothing at cut points to cope with the ill-conditioning arising from the tracking of the distance along geodesics. As an alternative to geodesic-following methods, [7] approximate the geodesic distance by means of the numerical solution of the heat kernel defined on the manifold. The cut locus is then identified as the set of points where the trace of the Hessian of the distance explodes, thus again requiring some sort of smooth-

ing for proper approximation. To overcome these limitations, in [8] the authors propose a characterization of the cut locus as the limit in the Hausdorff sense of a variationally-defined thawed region around the cut locus. This allows the construction of a convergent finite-element-based numerical approximation of the cut locus which is described and analyzed in [9].

In this paper we propose a novel characterization of the cut locus based on Optimal Transport (OT) theory and exploit it to derive a stable and accurate numerical method for its approximation on compact Riemannian manifolds, that, exploiting modern technology of numerical methods for PDEs, is more efficient than other methods present in literature. The cut locus has been used extensively together with its properties in the analysis of the regularity of optimal transport problems [10, 11, 12, 13]. On the other hand, to the best of our knowledge, our characterization of the cut locus has never been proposed before.

In OT problems, one looks for the optimal strategy to re-allocate a non-negative measure  $f^+$  into another non-negative measure  $f^-$  with equal mass, given a cost for transporting one unit of mass (see [14, 15, 16, 17] for a complete overview of the topic). When the transport takes place in a Riemannian manifold with the geodesic distance as cost, the solutions of the OT problem can be deduced from the solution of a nonlinear system of PDEs known as Monge-Kantorovich equations (MK equations). We denote the solution of the MK equations by  $(u^*, \mu^*)$ . The first element of the solution pair, the so-called *Kantorovich potential*  $u^*$ , is a continuous function with Lipschitz constant equal to 1, whose gradient is tangent to the paths (called rays) along which optimal transport movements occur, which are the geodesics [18]. The second solution element, the so-called *Optimal Transport Density* (OTD)  $\mu^*$ , is a non-negative measure on  $M$  that describes the mass flux through each portion of the manifold in an optimal transportation schedule from  $f^+$  into  $f^-$ .

A fundamental property of the OTD  $\mu^*$  is that it decays towards zero at the endpoints of the geodesics along which the mass is moved [19]. This fact suggests that if we take  $f^+ = dV_g(M)\delta_p$  and  $f^- = dV_g$  (where  $\delta_p$  denotes the Dirac measure centered at  $p$ ,  $dV_g$  the volume form induced by the metric  $g$ , and  $dV_g(M)$  is the measure of  $M$ ), the OTD restricted to all geodesics starting at point  $p$  tends to zero when approaching the points that form the cut locus of  $p$  in  $M$ . This intuition is confirmed by the following theorem, which represents our characterization of  $C_p$ :

**Theorem 1.** *Let  $(M, g)$  be a compact and geodesically complete Riemannian manifold of dimension  $n$  with no boundary. Given a point  $p \in M$ , the OTD  $\mu^*$  solution of the MK equations with  $f^+ = dV_g(M)\delta_p$  and  $f^- = dV_g$  admits, in the set  $M \setminus \{p\}$ , a continuous density  $\underline{\mu}$  with respect to the volume form  $dV_g$  whose zero set coincides with  $C_p$  i.e.,*

$$\mu^* = \underline{\mu} dV_g, \quad C_p = \{x \in M \setminus \{p\} : \underline{\mu}(x) = 0\}.$$

Based on this characterization, we propose a new variationally-based numerical scheme to approximate the cut locus on compact surfaces by means of the numerical solution of the MK equations. For the latter, we adopt the approach described in [20], where the discrete Dynamical Monge-Kantorovich (DMK) framework described in [21, 22] is extended to  $\mathbb{R}^3$ -embedded surfaces. We show the effectiveness of the proposed numerical approach identifying the cut locus of the following triangulated surfaces: a torus, for which the cut locus is known, and two test cases borrowed from [4] to show the applicability to generic surfaces.

The paper is organized as follows. First we present all the Riemannian objects required for the definition of the cut-locus, together with some of its properties. Then, in Section 3 we recall the definition of the Optimal Transport Problem with cost equal to the geodesic distance and the MK equations. Section 4 is dedicated to the connection of the MK equations with the cut-locus and ends with the proof of Theorem 1. Finally, Section 5 is dedicated to the presentation of the proposed numerical approach to identify the cut locus of triangulated surfaces via the DMK strategy and concludes with some numerical experiments.

## 2 The cut locus of a point on a Riemannian Manifold

We consider a geodesically complete and compact Riemannian manifold  $(M, g)$  with no boundary, equipped with a smooth metric  $g$ . We denote with  $\langle v, w \rangle_{g(x)}$  the application of the metric  $g$  evaluated at  $x$  to the two vectors  $v, w \in T_x M$ . The symbols  $\nabla_g$ ,  $|\cdot|_g$ , and  $dV_g$  are used to identify the gradient operator, the vector norm, and the volume form induced by the metric tensor  $g$  on  $M$ . The distance between two points  $x, y \in M$  is defined as:

$$\text{dist}_g(x, y) = \inf_{\sigma} \left\{ \int_0^1 \sqrt{\langle \dot{\sigma}(s), \dot{\sigma}(s) \rangle_{g(\sigma(s))}} ds : \begin{array}{l} \sigma \in \mathcal{C}^1([0, 1], M) \\ \sigma(0) = x, \sigma(1) = y \end{array} \right\}.$$

Given a point  $p \in M$ , we denote with  $\exp_p : T_p M \rightarrow M$  the exponential map of  $(M, g)$  at  $p$  and with  $\exp_p^{-1}$  its inverse, where well defined.

## 2.1 Cut locus of a point

We now give the definition and some properties of the cut locus  $C_p$  of a point  $p \in M$  and of all the related objects that will be used in the sequel (see [23]). Figure 1 illustrates graphically these definitions for a torus embedded in  $\mathbb{R}^3$ .

**Definition 1.** Let  $(M, g)$  be a compact and geodesically complete Riemannian manifold of dimension  $n$  and consider a point  $p \in M$ . Let  $U_p M$  be the set of unit tangent vectors at  $p$ , i.e.:

$$U_p M := \{ \theta \in T_p M : \langle \theta, \theta \rangle_{g(p)} = 1 \} .$$

The cut time  $\mathcal{T}_p(\theta)$  of  $\theta \in U_p M$  is defined as:

$$\mathcal{T}_p(\theta) := \sup \{ t \geq 0 : \exp_p(s\theta)_{0 \leq s < t} \text{ is a minimizing geodesic} \} . \quad (1)$$

The sets:

$$\hat{I}_p := \{ t\theta : \theta \in U_p M, 0 < t < \mathcal{T}_p(\theta) \} \subset T_p M \quad \text{and} \quad I_p := \exp_p(\hat{I}_p) \subset M \quad (2)$$

are called the injectivity domain and the interior set at  $p$ . Note that  $\exp_p$  is a diffeomorphism from  $\hat{I}_p$  to  $I_p$ , thus  $\exp_p^{-1}$  is defined from  $I_p$  to  $\hat{I}_p$ .

The sets:

$$\hat{C}_p := \{ \mathcal{T}_p(\theta)\theta : \theta \in U_p M \} \subset T_p M \quad \text{and} \quad C_p := \exp_p(\hat{C}_p) \subset M$$

are called, respectively, the tangent cut locus and the cut locus of  $p$ .

**Lemma 1** (Properties of the cut time [24]). *The functions  $\mathcal{T}_p$  and  $\mathcal{T}_p^{\mathcal{B}}$  defined in eqs. (1) and (4) are Lipschitz continuous.*

**Lemma 2** (Properties of the cut locus [23]). *The manifold  $M$  is the union of three disjoint sets: the point  $p$ , the interior set  $I_p$ , and the cut locus  $C_p$ . Moreover,  $C_p$  is a null set of the volume form  $dV_g$ .*

**Lemma 3** (Properties of the injectivity domain [23]). *The injectivity domain  $\hat{I}_p$  is a star shaped subset of  $T_p M$  with boundary given by  $\hat{C}_p$ .*

As an example, Figure 1 shows the cut locus  $C_p$  (red color) of a point  $p$  lying on the external ‘‘equator’’ of the torus (from [26, 25]) and an approximation of the tangent cut locus  $\hat{C}_p \subset T_p M$  (blue color) obtained by solving numerically the equations of the geodesic curves emanating from  $p = (3, 0, 0)$ .

## 2.2 Riemannian polar coordinates

Next we give workable expressions, in local coordinates, for these cut locus related quantities. To this aim, we need to fix proper charts and local coordinates. In view of lemma 3, it is convenient to use Riemannian polar coordinates (see [27]). However we need to be slightly pedantic here about their definition and properties because we will need to show that our solution of the OT problem is free of the singularities introduced by such coordinate systems).

Any set of these coordinates depends on the choice of a  $g(p)$ -orthonormal basis  $\mathcal{B} = \{e_1^{\mathcal{B}}, \dots, e_n^{\mathcal{B}}\}$  of  $T_p M$ , which allows the identification of  $T_p M$  with  $\mathbb{R}^n$  via the map  $v \mapsto (v_1^{\mathcal{B}}, \dots, v_n^{\mathcal{B}})$  with  $v_i^{\mathcal{B}} := \langle v, e_i^{\mathcal{B}} \rangle_{g(p)}$  for  $i = 1, \dots, n$ . We define the map

$$\Psi^{\mathcal{B}} : \hat{I}_p \rightarrow \mathbb{R}_+ \times \mathcal{S}^{n-1}, \quad v \mapsto \left( |v|_g, \frac{v^{\mathcal{B}}}{|v|_g} \right)$$

and, denoting  $\mathcal{S}_o^{n-1} = \mathcal{S}^{n-1} \setminus (0, \dots, \pm 1)$ , we introduce the (Euclidean) polar coordinates

$$P : \mathbb{R}_+ \times \mathcal{S}_o^{n-1} \rightarrow \mathbb{R}_+ \times \mathbb{U}^{n-1}, \quad \mathbb{U}^{n-1} = ]0, \pi[^{n-2} \times \mathcal{S}^1 \\ (r, y) \mapsto (r, \varphi_1(y), \dots, \varphi_{n-1}(y))$$

where  $\varphi = (\varphi_1, \dots, \varphi_{n-1})$  are the  $n - 1$  spherical coordinates parameterizing  $\mathcal{S}^{n-1}$  (see [28] for explicit formulas). Then, the Riemannian polar coordinates relative to the basis  $\mathcal{B}$  is the map  $\phi_p^{\mathcal{B}} = P \circ \Psi^{\mathcal{B}} \circ \exp_p$ . Explicitly, they are given by:

$$\phi_p^{\mathcal{B}} : I_p^{\mathcal{B}} \xrightarrow{\exp_p^{-1}} \hat{I}_p^{\mathcal{B}} \xrightarrow{\Psi^{\mathcal{B}}} \mathbb{R}_+ \times \mathcal{S}_o^{n-1} \xrightarrow{P} \mathbb{R}_+ \times \mathbb{U}^{n-1} \quad (3) \\ x \mapsto v := \exp_p(x) \mapsto \left( |v|_g, \frac{v^{\mathcal{B}}}{|v|_g} \right) \mapsto \left( |v|_g, \varphi \left( \frac{v^{\mathcal{B}}}{|v|_g} \right) \right)$$

where the sets  $I_p^{\mathcal{B}} \subset I_p$  and  $\hat{I}_p^{\mathcal{B}} \subset \hat{I}_p$  are the preimages under the maps  $\Psi^{\mathcal{B}} \circ \exp_p$  and  $\Psi^{\mathcal{B}}$  of  $\mathbb{R}_+ \times \mathcal{S}_o^{n-1}$ , respectively. Note that  $|v|_g = \text{dist}_g(p, x)$ .

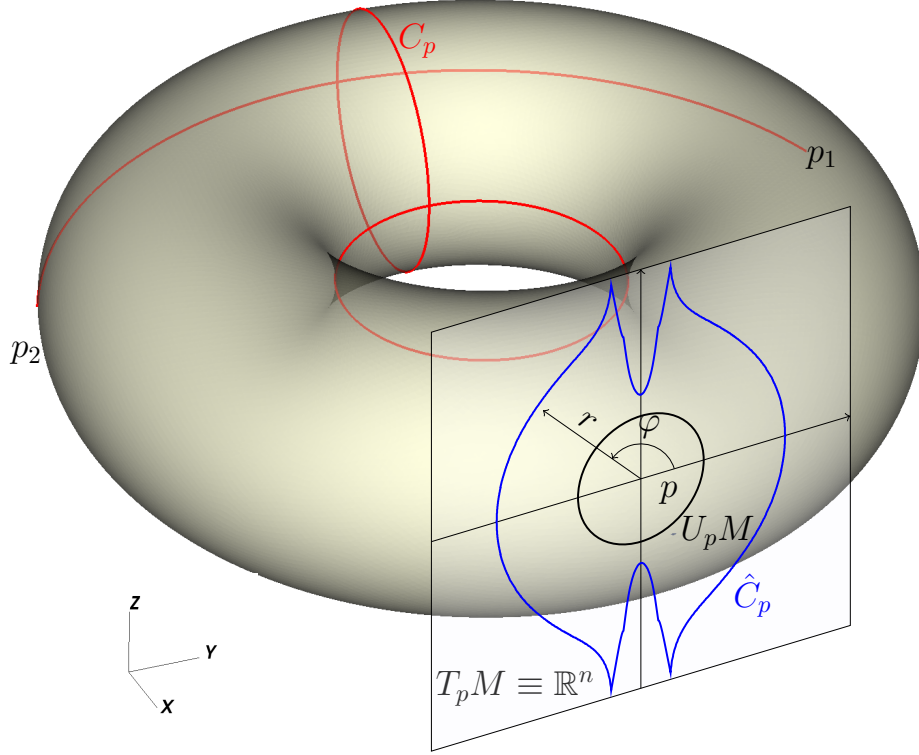


Figure 1: The tangent cut locus and the cut locus of a point on the torus with major and minor radi  $r_{\max} = 2$  and  $r_{\min} = 1$  embedded in  $\mathbb{R}^3$ . The red curves identify the cut locus of the point  $p = (R, 0, 0)$  with  $R := r_{\max} + r_{\min}$  located on the external “equator”. Note that the cut locus is formed by the internal “equator”, the opposite “meridian”, and a portion of the external “equator” connecting the two points  $p_1 = (R \cos(\alpha), R \sin(\alpha), 0)$  and  $p_2 = (R \cos(\alpha), -R \sin(\alpha), 0)$  with  $\alpha = \pi r_{\min} / \sqrt{R r_{\min}}$  (formulae taken from [25, Theorem 9]). The blue lines represent an approximation of the tangent cut locus  $\hat{C}_p$  obtained by straight-forward numerical approximation of the geodesics emanating from  $p$ .

**Remark 1.** The set  $I_p^{\mathcal{B}}$  coincides with  $I_p$  minus a geodesic curve which passes through  $p$  and depends on the basis  $\mathcal{B}$ .

It is clear that, given  $\mathcal{B}$ , there exists a one-to-one correspondence between elements of  $U_p M \setminus \{e_n^{\mathcal{B}}, -e_n^{\mathcal{B}}\}$  and  $\mathbb{U}^{n-1}$ . Thus, we define the cut time function  $\mathcal{T}_p^{\mathcal{B}}$  that maps the angle variables  $\varphi$  into the cut time of the corresponding unit vector in the tangent space i.e.,

$$\mathcal{T}_p^{\mathcal{B}} : \mathbb{U}^{n-1} \rightarrow \mathbb{R}_+, \quad \mathcal{T}_p^{\mathcal{B}}(\varphi) := \mathcal{T}_p \circ (\Psi^{\mathcal{B}})^{-1} \circ P^{-1}(1, \varphi) \quad \forall \varphi \in \mathbb{U}^{n-1} \quad (4)$$

**Lemma 4** (Properties of polar coordinates, [27]). *For any  $g(p)$ -orthonormal basis  $\mathcal{B}$ , the matrix representing the metric  $g|_{I_p^{\mathcal{B}}}$  written in Riemannian polar coordinates has the block-diagonal expression*

$$g^{\mathcal{B}}(r, \varphi) = \begin{pmatrix} 1 & 0 \\ 0 & h^{\mathcal{B}}(r, \varphi) \end{pmatrix},$$

where  $h^{\mathcal{B}}(r, \varphi)$  is a  $(n-1) \times (n-1)$  symmetric and positive-definite matrix.

We denote

$$\mathcal{J}^{\mathcal{B}}(r, \varphi) dr \wedge d\varphi_1 \wedge \dots \wedge d\varphi_{n-1}$$

the volume form  $dV_g$  expressed in polar coordinates in the interior set  $I_p$ .

**Lemma 5.** *The function  $\mathcal{J}^{\mathcal{B}}$  factorizes as follows*

$$\mathcal{J}^{\mathcal{B}}(r, \varphi) = G^{\mathcal{B}}(r, \varphi) J(r, \varphi), \quad (5)$$

where  $G^{\mathcal{B}} : \mathbb{R}_+ \times \mathbb{U}^{n-1} \rightarrow \mathbb{R}_+$  is given by

$$G^{\mathcal{B}}(r, \varphi) = \sqrt{\det(g \circ (\phi_p^{\mathcal{B}})^{-1}(r, \varphi))} \quad (6)$$

and  $J$  is the absolute value of the determinant of the Jacobian matrix of  $P^{-1}$  and is given by:

$$J(r, \varphi^1, \varphi^2, \dots, \varphi^{n-2}) = r^{n-1} \sin^{n-2}(\varphi_1) \sin^{n-3}(\varphi_2) \dots \sin(\varphi_{n-2}). \quad (7)$$

*Proof.* The proof comes directly from the appropriate composition of the relevant functions defined above.  $\square$

Let  $SO(n, T_p M)$  be the set of all proper ( $\det = +1$ ) linear  $g(p)$ -isometries of  $T_p M$ . Given a  $g(p)$ -orthonormal basis  $\mathcal{B} = \{e_1^{\mathcal{B}}, \dots, e_n^{\mathcal{B}}\}$  of  $T_p M$ , we associate to any  $\hat{R} \in SO(n, T_p M)$  the matrix  $R^{\mathcal{B}} \in SO(n)$  with entries  $R_{i,j}^{\mathcal{B}} = \langle e_i^{\mathcal{B}}, \hat{R}e_j^{\mathcal{B}} \rangle_{g(p)}$ . Also, we denote by  $\hat{R}\mathcal{B}$  the rotated basis  $\{\hat{R}e_1^{\mathcal{B}}, \dots, \hat{R}e_n^{\mathcal{B}}\}$ .

**Lemma 6.** For any  $g(p)$ -orthonormal basis  $\mathcal{B}$  and any  $\hat{R} \in SO(n, T_p M)$ ,

$$G^{\hat{R}\mathcal{B}} \circ P(r, R^{\mathcal{B}}y) = G^{\mathcal{B}} \circ P(r, y)$$

for all  $r \in \mathbb{R}_+$  and  $y \in \mathcal{S}_o^{n-1}$  such that  $(\hat{R})^T y \in \mathcal{S}_o^{n-1}$ .

*Proof.* This follows from the fact that, as we verify,

$$\left(\Psi^{\hat{R}\mathcal{B}}\right)^{-1}(r, R^{\mathcal{B}}y) = \left(\Psi^{\mathcal{B}}\right)^{-1}(r, y) \quad (8)$$

for all  $r, y$  as in the statement. Write for short  $R$  for  $R^{\mathcal{B}}$ . First note that,  $\forall v \in T_p M$ ,  $v^{\hat{R}\mathcal{B}} = R^T v^{\mathcal{B}}$  and  $(\hat{R}v)^{\mathcal{B}} = Rv^{\mathcal{B}}$ . Thus

$$\begin{aligned} \Psi^{\hat{R}\mathcal{B}}(\hat{R}v) &= \left(|\hat{R}v|_g, \frac{(\hat{R}v)^{\hat{R}\mathcal{B}}}{|\hat{R}v|_g}\right) = \left(|v|_g, \frac{R^T(\hat{R}v)^{\mathcal{B}}}{|v|_g}\right) \\ &= \left(|v|_g, \frac{R^T Rv^{\mathcal{B}}}{|v|_g}\right) = \Psi^{\mathcal{B}}(v). \end{aligned}$$

This implies that, if  $(r, y) = \Psi^{\mathcal{B}}(v)$  then

$$\begin{aligned} \Psi^{\hat{R}\mathcal{B}} \circ \left(\Psi^{\mathcal{B}}\right)^{-1}(r, y) &= \Psi^{\hat{R}\mathcal{B}}(v) = \left(|v|_g, \frac{v^{\hat{R}\mathcal{B}}}{|v|_g}\right) \\ &= \left(|v|_g, \frac{Rv^{\mathcal{B}}}{|v|_g}\right) = (r, Ry), \end{aligned}$$

namely eq. (8).  $\square$

### 3 Monge-Kantorovich equations on manifolds

In this section we present the Monge-Kantorovich equations (MK equations), an equivalent PDE formulation of the optimal transport problem on a Riemannian manifold with geodesic distance as transport cost. We use the formulation described in [29, 18], assuming that one of the transported measures  $f^+$  and  $f^-$  on  $M$  admits a density with respect to the volume form  $dV_g$ . Under these assumptions the MK equations can be written as the problem of finding a pair  $(u^*, \mu^*)$ , where  $u^*$  is a continuous function with Lipschitz constant equal to 1 and  $\mu^*$  is a non-negative measure, that solves

$$-\operatorname{div}_g(\mu^* \nabla_g u^*) = f^+ - f^- \quad \text{on } M \quad (9a)$$

$$|\nabla_g u^*|_g \leq 1 \quad \text{on } M \quad (9b)$$

$$|\nabla_g u^*|_g = 1 \quad \mu^* - a.e. \quad (9c)$$

where eq. (9a) must be interpreted in the following weak form:

$$\int_M \langle \nabla_g u^*, \nabla_g \phi \rangle_g d\mu^* = \int_M \phi df^+ - \int_M \phi df^-, \quad \forall \phi \in \mathcal{C}^1(M). \quad (10)$$

The components of the solution pair  $(u^*, \mu^*)$  of the above system are named Kantorovich potential and OTD, respectively.

The following lemma summarizes a series of results on the solution of the MK equations from [30, 31, 14, 32, 33, 18].

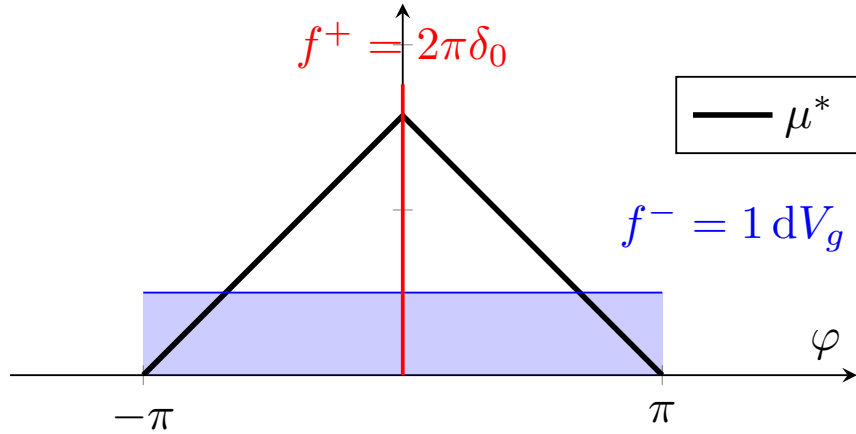


Figure 2: Graph of the OTD  $\mu^*$  (black) solution of the MK equations in the unit circle  $\mathcal{S}^1$  (the point  $-\pi$  is identified with  $\pi$ ) with  $f^+ = 2\pi\delta_0$  (red) and  $f^- = d\varphi$  (blue)

**Lemma 7** (Properties of Monge-Kantorovich equations). *The Kantorovich potential  $u^*$  is unique up to a constant within the support of  $\mu^*$  (outside  $\text{supp}(\mu^*)$  there exist infinitely many functions  $u$  that satisfy eq. (9) [19]).*

*If either  $f^+$  or  $f^-$  (or both) is absolutely continuous with respect to the volume form  $dV_g$ , then the OTD  $\mu^*$  is unique and is absolutely continuous with respect to  $dV_g$ .*

**Remark 2.** *Without a priori knowledge of the integrability of  $\mu^*$ , guaranteed by lemma 7 in our problem, the formulation of the MK equations requires the notion of gradient with respect to measure [29].*

Intuitively speaking, the link between OT and the solution  $(u^*, \mu^*)$  of the MK equations eq. (9) is as follows. The OTD  $\mu^*$  can be seen as a measure of the flux through each portion of the manifold in the optimal reallocation of  $f^+$  into  $f^-$ . Mass moves along disjoint transport rays that follow the direction of the gradient of the Kantorovich potential  $u^*$ . Intuitively, these transport rays are geodesics connecting points in the support of  $f^+$  with points in the support of  $f^-$  (we refer the reader to [14] for the proper definition of transport rays). Under certain properties of the transported measures  $f^+$  and  $f^-$  ( $L^\infty$  densities and disjoint supports), [19] proved that the OTD tends to zero at the endpoints of each transport ray.

#### 4 OT characterization of $C_p$

From the property of the decay of the OTD along the transport rays we devise the following strategy for the search of the cut locus: we set  $f^+ = dV_g(M)\delta_p$  (with  $\delta_p$  the Dirac delta centered at  $p$ ) and  $f^- = dV_g$  and look at the zero-set of  $\mu^*$ . The intuition is that in the optimal reallocation of the Dirac mass centered at  $p$ , the mass is “sent” from  $p$  to all the points of  $M$  along geodesics. The mass is progressively “absorbed” by the constant sink term  $f^- = dV_g$  until we reach those points where mass is coming also from a different direction. At those points,  $\mu^*$  becomes zero. For a cleaner understanding of this idea and of the properties of the OTD, we present a simple example on the unit circle  $\mathcal{S}^1$ .

**Example 1.** *On the unit circle  $\mathcal{S}^1 = \{x^2 + y^2 = 1\}$  we consider the point  $p = (1, 0)$  and source terms given by  $f^+ = 2\pi\delta_p$  and  $f^- = 1d\varphi$ . Using the angle coordinate  $\varphi \in \mathcal{S}^1$  the Kantorovich potential and the OTD are given by:*

$$u^*(\varphi) = -|\varphi|, \quad \mu^*(\varphi) = \pi - |\varphi|, \quad \varphi \in \mathcal{S}^1. \quad (11)$$

*The graphs of  $\mu^*$  and the transported measures are reported in Figure 2. The OTD  $\mu^*$  progressively decays moving away from the point  $p$ , until the antipodal point is reached, where it vanishes. According to the definition given in [14], in this example the arcs  $]-\pi, 0[$  and  $]0, \pi[$  are the transport rays.*

The extension of this idea to a general manifold leads to the following theorem, which is a more complete version of Theorem 1.

**Theorem 2.** *Let  $(M, g)$  be a compact and geodesically complete Riemannian manifold of dimension  $n$  and with no boundary. Consider a point  $p \in M$  and the measures*

$$f^+ = dV_g(M)\delta_p, \quad f^- = dV_g. \quad (12)$$

*Let  $(u^*, \mu^*)$  be the solution of the MK equations with measures given by eq. (12). Then :*

*i) the Kantorovich Potential  $u^*$  coincides with minus the geodesic distance from  $p$ :*

$$u^*(x) = -\text{dist}_g(x, p); \quad (13)$$

*ii) when restricted to  $M \setminus \{p\}$ , the OTD  $\mu^*$  admits a continuous density  $\underline{\mu}$  with respect to the volume form  $dV_g$ :*

$$\mu^* = \underline{\mu} dV_g, \quad \underline{\mu} \in C^0(M \setminus \{p\});$$

*iii) the zero set of  $\underline{\mu}$  coincides with the cut locus  $C_p$  of  $p$ :*

$$C_p = \{x \in M \setminus \{p\} : \underline{\mu}(x) = 0\};$$

*iv) for any  $g(p)$ -orthonormal basis  $\mathcal{B}$ , the local representative  $\underline{\mu}^{\mathcal{B}} := \underline{\mu} \circ (\phi_p^{\mathcal{B}})^{-1}$  in the chart  $\phi_p^{\mathcal{B}}$  of the function  $\underline{\mu}$  is given by*

$$\underline{\mu}^{\mathcal{B}}(r, \varphi) = \frac{1}{G^{\mathcal{B}}(r, \varphi)r^{n-1}} \int_r^{\mathcal{T}_p^{\mathcal{B}}(\varphi)} G^{\mathcal{B}}(s, \varphi)s^{n-1} ds, \quad (14)$$

*for all  $(r, \varphi) \in \phi_p^{\mathcal{B}}(I_p^{\mathcal{B}}) \subset \mathbb{R}_+ \times \mathbb{U}^{n-1}$ .*

*Proof.* We first observe that thanks to lemma 6, given two  $g(p)$ -orthonormal basis  $\mathcal{B}$  and  $\mathcal{B}'$  the functions  $\underline{\mu}^{\mathcal{B}} \circ \phi_p^{\mathcal{B}}$  and  $\underline{\mu}^{\mathcal{B}'} \circ \phi_p^{\mathcal{B}'}$  coincide in the intersection of their domains. Therefore, there exists a *continuous* function  $\underline{\mu}$  on  $I_p$  with local representative  $\underline{\mu}^{\mathcal{B}}$  in any chart  $\phi_p^{\mathcal{B}}$  given by eq. (14). Moreover, since for every  $\mathcal{B}$   $\underline{\mu}^{\mathcal{B}}$  is positive in its domain  $\phi_p^{\mathcal{B}}(I_p^{\mathcal{B}})$  and, for every  $\varphi$ ,

$$\lim_{r \rightarrow \mathcal{T}_p^{\mathcal{B}}(\varphi)} \underline{\mu}^{\mathcal{B}}(r, \varphi) = 0,$$

the function  $\underline{\mu}$  admits a (unique) continuous extension on  $I_p \cup C_p = M \setminus \{p\}$ , which we will continue to denote with  $\underline{\mu}$ , which is non-negative and whose zero set coincides with the cut locus of  $p$ . This proves statements iii. The term  $G^{\mathcal{B}}$ , defined in eq. (6), is clearly bounded from above and from below. Hence, the integral in eq. (14) tends to zero as  $r \rightarrow \mathcal{T}_p^{\mathcal{B}}(\varphi)$ .

Now, we note that the source term  $f^-$  in eq. (12) is absolutely continuous with respect to the volume form  $dV_g$ . Thus, lemma 7 ensures that the OTD  $\mu^*$  admits a unique density with respect to the volume form  $dV_g$ . We now show that, with  $\underline{\mu}$  defined above, the pair  $(u^*, \mu^*)$  given by

$$u^*(x) = -\text{dist}_g(x, p), \quad \mu^* \stackrel{\text{a.e.}}{=} \underline{\mu} dV_g \quad (15)$$

solves eq. (9). It is clear that  $u^*$  satisfies the constraints in eqs. (9b) and (9c). Thus, we only have to prove that  $(u^*, \mu^*)$  solves eq. (10) for  $f^+$  and  $f^-$  in eq. (12) i.e.,

$$\int_M \langle \nabla_g u^*, \nabla_g \phi \rangle_g d\mu^* = \int_M (dV_g(M))\phi\delta_p - \int_M \phi dV_g \quad \forall \phi \in C^1(M). \quad (16)$$

For all  $\phi \in C^1(M)$ , the right-hand side *RHS* of the above equation can be evaluated as

$$RHS = (dV_g(M))\phi(p) - \int_M \phi dV_g. \quad (17)$$

We know, from lemma 2 and remark 1, that for any  $g(p)$ -orthonormal basis  $\mathcal{B}$  the set  $M \setminus I_p^{\mathcal{B}}$  has zero measure on  $M$ . Thus, we can restrict the integrals on the left-hand side of eq. (16) to  $I_p^{\mathcal{B}}$  and use the Riemannian polar coordinates to compute them. Write  $\phi^{\mathcal{B}} = \phi \circ (\phi_p^{\mathcal{B}})^{-1}$  and  $u^{\mathcal{B}} = u^* \circ (\phi_p^{\mathcal{B}})^{-1}$ . Thus,  $u^{\mathcal{B}}(r, \varphi) = -r$  and the left-hand side *LHS* of eq. (16) becomes:

$$LHS = \int_{\mathbb{U}^{n-1}} \int_0^{\mathcal{T}_p^{\mathcal{B}}(\varphi)} \nabla u^{\mathcal{B}}(r, \varphi) \cdot g^{\mathcal{B}}(r, \varphi)^{-1} \nabla \phi^{\mathcal{B}}(r, \varphi) \underline{\mu}^{\mathcal{B}}(r, \varphi) \mathcal{J}^{\mathcal{B}}(r, \varphi) dr d\varphi.$$

Now,  $\nabla u^{\mathcal{B}}(r, \varphi) = (-1, 0, \dots, 0)$  and from lemma 4 we have

$$\nabla u^{\mathcal{B}}(r, \varphi) \cdot g^{\mathcal{B}}(r, \varphi)^{-1} \nabla \phi^{\mathcal{B}}(r, \varphi) = -\partial_r \phi^{\mathcal{B}}(r, \varphi).$$

Thus, recalling eq. (14) and eq. (5) of lemma 5

$$LHS = - \int_{\mathbb{U}^{n-1}} \int_0^{\mathcal{T}_p^{\mathcal{B}}(\varphi)} \left( \int_r^{\mathcal{T}_p^{\mathcal{B}}(\varphi)} \mathcal{J}^{\mathcal{B}}(s, \varphi) ds \right) \partial_r \phi^{\mathcal{B}}(r, \varphi) dr d\varphi.$$

Integration by parts yields:

$$\begin{aligned} LHS &= - \int_{\mathbb{U}^{n-1}} \left( \left[ \left( \int_r^{\mathcal{T}_p^{\mathcal{B}}(\varphi)} \mathcal{J}^{\mathcal{B}}(s, \varphi) ds \right) \phi^{\mathcal{B}}(r, \varphi) \right]_0^{\mathcal{T}_p^{\mathcal{B}}(\varphi)} \right) d\varphi \\ &\quad + \int_{\mathbb{U}^{n-1}} \left( \int_0^{\mathcal{T}_p^{\mathcal{B}}(\varphi)} \partial_r \left( \int_r^{\mathcal{T}_p^{\mathcal{B}}(\varphi)} \mathcal{J}^{\mathcal{B}}(s, \varphi) ds \right) \phi^{\mathcal{B}}(r, \varphi) dr \right) d\varphi. \end{aligned}$$

The first term is evaluated by taking the separate limits as  $r \rightarrow \mathcal{T}_p^{\mathcal{B}}(\varphi)$  and as  $r \rightarrow 0$ , with the former yielding zero. In conclusion,

$$\begin{aligned} LHS &= \phi(p) \int_{\mathbb{U}^{n-1}} \int_0^{\mathcal{T}_p^{\mathcal{B}}(\varphi)} \mathcal{J}^{\mathcal{B}}(s, \varphi) ds d\varphi - \int_{\mathbb{U}^{n-1}} \int_0^{\mathcal{T}_p^{\mathcal{B}}(\varphi)} \mathcal{J}^{\mathcal{B}}(r, \varphi) \phi^{\mathcal{B}}(r, \varphi) dr d\varphi \\ &= (dV_g(M))\phi(p) - \int_{I_p^{\mathcal{B}}} \phi dV_g, \end{aligned}$$

and then  $LHS = RHS$  for all  $\phi \in \mathcal{C}^1(M)$ , proving eq. (16). This shows that the pair  $(u^*, \mu^*)$  in eq. (15) solves of the MK equations for  $f^+$  and  $f^-$  in eq. (12). This proves statements i,ii, and iv. Statement iii has already been proved.  $\square$

**Remark 3.** *It is worth noting that, thanks to Theorem 2 and to the results in [21], we can give a variational characterization of the OTD as the minimizer of:*

$$\min_{\mu} \{ \mathcal{L}_g(\mu) : \mu \in \mathcal{C}^0(M \setminus \{p\}, \mathbb{R}_+) \}$$

with  $\mathcal{L}_g = \mathcal{E}_g + \mathcal{M}_g$  and

$$\begin{aligned} \mathcal{E}_g(\mu) &:= \sup_{\phi \in \text{Lip}(M)} \left\{ \int_M (dV_g(M)\delta_p - dV_g)\phi - \mu \frac{|\nabla_g \phi|^2}{2} dV_g \right\} \\ \mathcal{M}_g(\mu) &:= \frac{1}{2} \int_M \mu dV_g. \end{aligned}$$

This provides a variational characterization of the cut locus of a point  $p \in M$  as the zero set of the minimizer  $\mu^*$  of  $\mathcal{L}_g(\mu)$ .

## 5 Numerical approximation of the cut locus

In this section we present our strategy for the calculation of the cut locus based on Theorem 2. Unfortunately, it is numerically challenging to look directly at the zero set of the expression for OTD  $\mu^*$  given in eq. (14). Indeed, this would require the approximation of the distance and cut time functions, i.e. the same unknowns in the identification problem of the cut locus. As an alternative, at least in the case of a surface  $\Gamma$  embedded in  $\mathbb{R}^3$ , we approach the numerical solution of the MK equations eq. (9) by means of the ‘‘dynamic’’ reformulation of the MK equations, called DMK, recently proposed in [22], and its finite-element-based discretization, described in [21]. More precisely, we use the extension to the surface setting of the DMK approach as described in [20], in which the numerical schemes developed in [21] are extended to the surface setting using the Surface Finite Element Method (SFEM) framework reviewed in [34].

We summarize here the fundamental steps of SFEM-DMK that impact on our goal of calculating the cut locus. First, the surface  $\Gamma$  is decomposed with a geodesic triangulation  $\Gamma = \mathcal{T}(\Gamma)$ , formed by triangles whose edges are the geodesics between the vertices. Next, this triangulation is approximated by its piecewise linear interpolant  $\Gamma_h =$



$\mathcal{T}_h(\Gamma) = \cup \mathbb{E}_r$ , i.e., the union of 2-simplices  $\mathbb{E}_r$  in  $\mathbb{R}^3$  having the same vertices as  $\mathcal{T}(\Gamma)$  (for more details see [35, 34]). Using  $\Gamma_h$  it is possible to define appropriate discrete geometric quantities, such as surface gradients and discrete finite element function spaces, that allow the numerical discretization of the MK equations on surfaces embedded in  $\mathbb{R}^3$ . We refer to [34] for details on SFEM and to [20] for details and application examples of SFEM to the DMK on surfaces.

In practice, the calculation of the cut locus takes place on the piecewise linear interpolation  $\Gamma_h$  of  $\Gamma$  by means of the SFEM discretization of the MK equations with  $f^+ = dV_g(\Gamma_h)\delta_p$  and  $f^- = dV_g$ . To maintain stability we follow the procedure described in [21] whereby the Kantorovich potential  $u^*$  is interpolated on a uniformly refined mesh  $\mathcal{T}_{h/2}(\Gamma_h) \subset \mathcal{T}_h(\Gamma_h)$  by piecewise linear polynomials, while the OT density  $\mu^*$  is approximated on  $\mathcal{T}_h(\Gamma_h)$  by piecewise constants. As a consequence, the approximated cut locus is formed by the union of the triangles  $\mathbb{E}_r \in \mathcal{T}_h(\Gamma_h)$  where our numerically evaluated OTD,  $\mu_h^*$ , is close to zero. Thus, we give the following definition of the approximate cut locus ( $C_{p,h,\epsilon}$ ):

$$C_{p,h,\epsilon} := \{\cup \mathbb{E}_r \in \mathcal{T}_h(\Gamma_h) \text{ s.t. } (\mu_h^*)|_{\mathbb{E}_r} \leq \epsilon\}$$

where  $\epsilon$  is an appropriate preselected tolerance.

**Remark 1.** *The definition of this tolerance is crucial for a proper approximation of  $C_p$ . Indeed, it is rather difficult to approximate a one-dimensional structure, and more so single points, as a union of triangles of  $\mathcal{T}_h(\Gamma)$ , and we will see by experimentation that different values of  $\epsilon$  lead to different  $C_{p,h,\epsilon}$ . Another difficulty arises from the use of the singular source term  $f^+ = dV_g(\Gamma)\delta_p$ , which does not belong to the dual of  $H^1(\Gamma)$ . This is a typical problem in applications and yields suboptimal SFEM convergence rates for  $u^*$ . To address this issue one may either use regularization along the lines of [36, 37] or a posteriori error estimations to adapt the surface mesh. We choose not to employ any of these approaches since first order global accuracy is in any case enforced by the piecewise constant discretization of  $\mu^*$ .*

We would like to note that according to [38] the cut locus is stable under  $\mathcal{C}^2$  perturbations of the domain or of the metric but stability may be lost in case of  $\mathcal{C}^1$  perturbations. However, the ensuing experimental results show that our piecewise constant approximation of the transport density introduces enough regularization to our numerical solution, at least for the sample problems addressed in this work.

## 5.1 Numerical experiments

First we would like to note that a Python notebook reproducing the experiments presented in this section can be found at this link <https://doi.org/10.5281/zenodo.5710660>. The source code is available at the following [https://gitlab.com/enrico\\_facca/dmk\\_solver](https://gitlab.com/enrico_facca/dmk_solver) (subdirectory FaccaBertiFassoPutti2021\_CutLocus).

The first test case concerns the example described in Section 2.1 and shown in Figure 1 and deals with the calculation of the cut locus  $C_p$  of a torus  $T$  with radii  $r_{\max} = 2$  and  $r_{\min} = 1$  with respect to the point  $p = (3, 0, 0)$ . The results of our simulations are shown in Figure 3. The top panels of the figure depict the  $C_{p,h,\epsilon}$  obtained using a tolerance  $\epsilon = 10^{-3}$  on four refinement levels. It is clear that  $C_{p,h,\epsilon}$  approximates the real cut locus with satisfactory accuracy already on the coarsest grid, with progressively improving resolution as expected by the higher refinement levels. The effect of the mesh finite size is clearly discernible but no instabilities in the identification of the cut locus are visible. Note that perturbations of  $\Gamma$  and  $g$  in the refinement step from  $\mathcal{T}_h(\Gamma)$  to  $\mathcal{T}_{h/2}(\Gamma)$  are not strictly  $\mathcal{C}^{1,1}$ -regular. However, we can view  $\mathcal{T}_h(\Gamma)$  as a linear interpolation of  $\Gamma$  whose error can be bounded by  $h^2$  times the norm of the second fundamental form of  $\Gamma$  [35, 34, 39]. This regularity is sufficient to provide empirical justification of the stability of our calculations. This rationale is further strengthened by the results at the finest grid level.

The  $C_{p,h,\epsilon}$  for  $\epsilon = 10^{-4}$  is shown in the bottom panel of Figure 3. A much better approximation of the real cut locus is displayed with increased level of details. However, one portion of the ‘‘internal equator’’ opposite to  $p$  is not identified. We can give a heuristic explanation for this phenomenon by looking at the explicit formula of the OTD in eq. (14). Roughly, this formula predicts an increased value of the OTD in the regions of larger mass fluxes. In our case this corresponds to the region surrounding the internal equator, where the geodesics starting at  $p$  arrive with a small angle with respect to the internal great circle. Thus, the values of  $\mu_h^*$  in these triangles are relatively large, and the approximation of the cut locus becomes problematic when using an absolute identification criterion. This problem could of course be relieved by employing standard strategies that combine relative error measures and adaptive mesh refinements, tasks that go beyond the purpose of this paper.

The second test case is taken from [4, Section 5] where the authors consider the triaxial ellipsoid given by

$$E := \{(x, y, z) \in \mathbb{R}^3 : (x/0.2)^2 + (y/0.6)^2 + z^2 = 1\}.$$

The cut loci of two points in  $E$  are studied. The first point considered is  $p^1 = (-0.115470, 0, 0.816497)$ , an umbilic point whose cut locus consists of a single point. The second cut locus is relative to the point  $p^2 =$

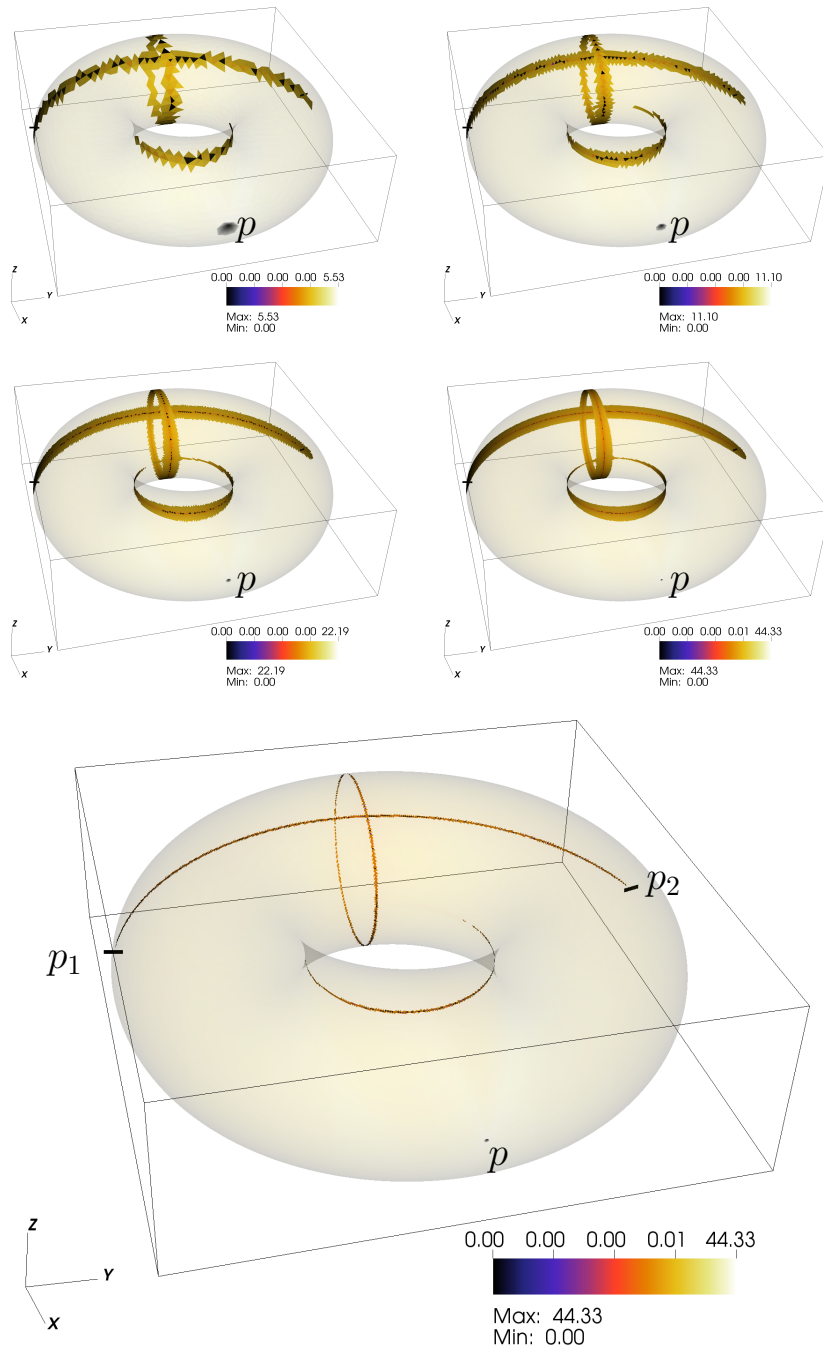


Figure 3: Numerical identification of the  $C_{p,h,\epsilon}$  of a torus obtained at four uniform mesh refinement levels for  $\epsilon = 0.001$ . The color map refers to  $\mu_h^*$  values. The coarsest mesh level contains 2712 nodes and 5424 triangles. The two segments in black intersect the surface of the torus at points  $p_1$  and  $p_2$  described in Figure 1. The bottom panel shows the  $C_{p,h,\epsilon}$  for  $\epsilon = 0.0001$  on the finest grid level.

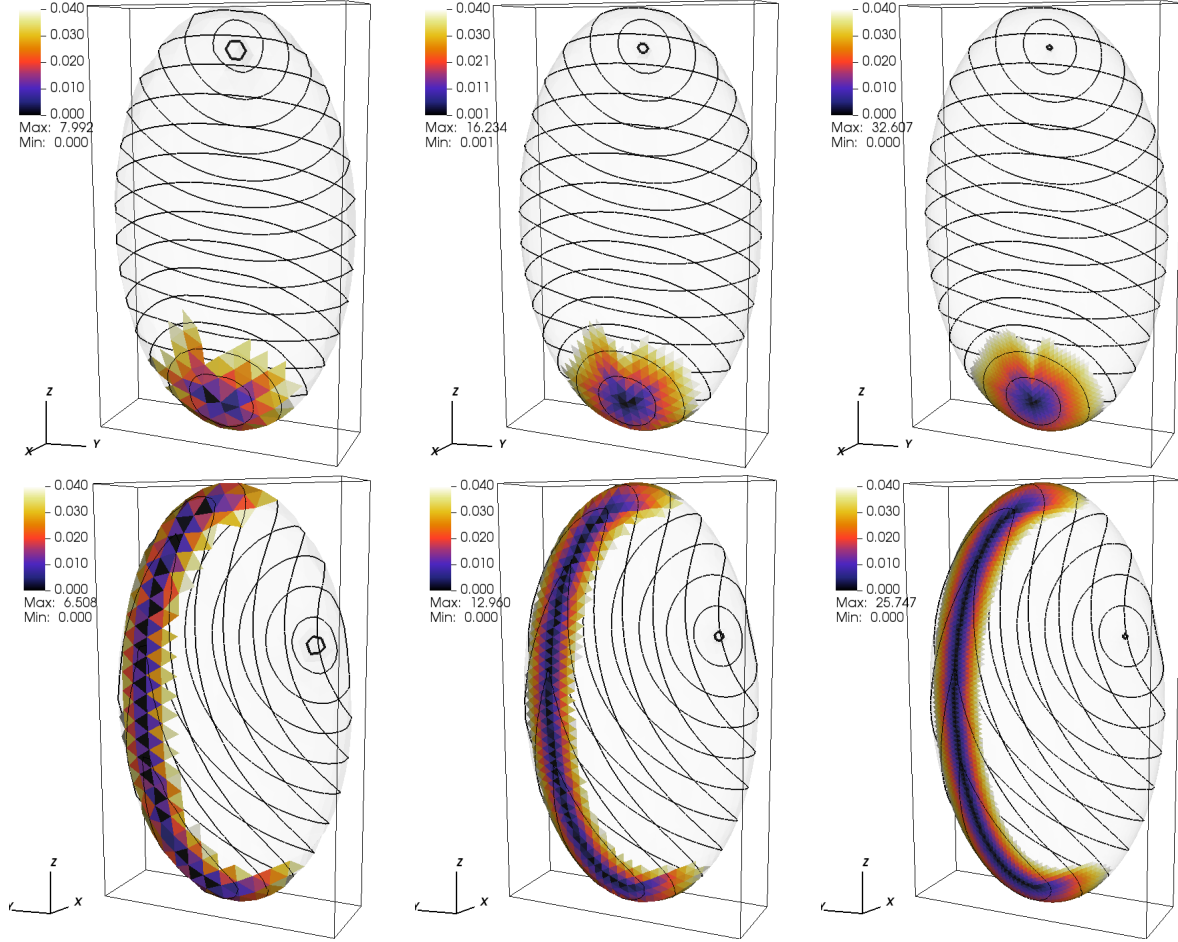


Figure 4: Ellipsoid  $(x/0.2)^2 + (y/0.6)^2 + (z)^2 = 1$ . The upper panels reports the spatial distribution of  $\mu_h^*$  for the point  $p^1 = (-0.115470, 0, 0.816497)$ . We report the results for three meshes, one the conformal refinement of the other, with the first having 534 nodes and 1064 triangles, and the latter 8514 nodes 17024 triangles. The point  $p^1$  is located “behind” the visible ellipsoid and it is marked with a black circle. We report only those triangles where  $\mu_h^*$  is below 0.04. We also report the contour lines of  $u_h^*$ . On the lower panels we report the same plots for the  $p^2 = (-0.151128, -0.350718, 0.295520)$ .

$(-0.151128, -0.350718, 0.295520)$  and is conjectured to be an arc on the opposite site of the ellipsoid [4, Conjecture 5.2]. In Figure 4 we report the spatial distribution of the approximate OTD  $\mu_h^*$  associated to the points  $p^1$  and  $p^2$ , on the top and bottom panels, respectively. We start from an initial triangulation  $\mathcal{T}_h$  of the ellipsoid with 534 nodes and 1064 triangles, obtained by means of the software described in [40]. We generate a sequence of finer grids conformally refining  $\mathcal{T}_h$  and “lifting” the added nodes (the mid-points of the edges of the triangles) to the ellipsoid. We report the spatial distribution of  $\mu_h^*$  only on those triangles where it is below the threshold  $\mu_h^* < 0.04$  to appreciate the decay of the OTD as it approaches the cut locus. Already at the coarsest grid, the region where  $\mu_h^*$  attains the lowest values (in black in Figure 4) strongly resembles the approximate cut locus computed in [4].

The final test-case, again taken from [4], looks for the cut locus of the quartic equation defined by

$$Q := \{(x, y, z) \in \mathbb{R}^3 : x^4 + y^4 + z^4 = 1\}$$

with respect to the point  $p = (0.533843, 0.800764, 0.844080)$ . Figure 5 shows the spatial distribution of  $\mu_h^*$  obtained on two different triangulations. The first mesh (left panel) is characterized by 34178 nodes and 68352 triangles in  $\mathcal{T}_h$ , where  $\mu_h^*$  is defined, and 136712 nodes and 273408 triangles, in  $\mathcal{T}_{h/2}$ , where  $u_h^*$  lives. The second mesh level (right panel) is exactly four times larger. The approximate zero set of  $\mu_h^*$  shown on the two refinements in Figure 5 compares well with the approximate cut locus reported in [4].

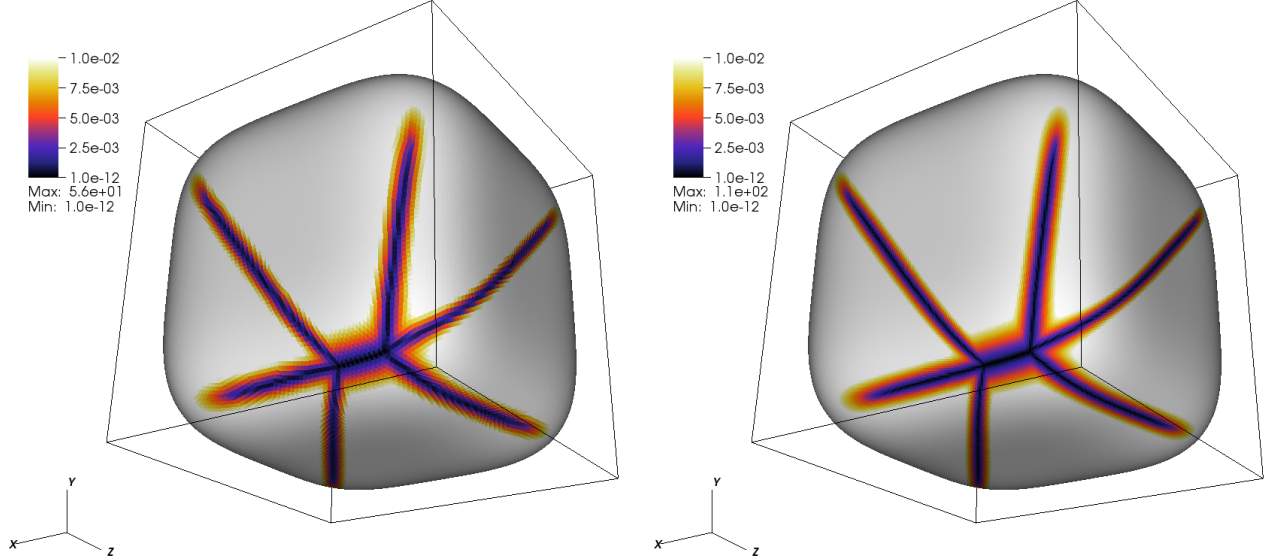


Figure 5: Spatial distribution of the  $\mu_h^*$  on the surface  $Q$  using  $f^+ = |Q|\delta_p$  with  $p = (0.533843, 0.800764, 0.844080)$  and  $f^- = 1$ . The left panel reports the result using a mesh containing 34178 nodes and 68352 cells. The color scale has its maximum at 0.01 to highlight the region where  $\mu_h^*$  attains the lowest value. The right panel reports the same results using the conformal refinement of the surface triangulation (136706 nodes and 273408 cells).

We would like to note here that our DMK-based approach is much more computationally efficient than [4]. Indeed, the computational cost for these simulations on a laptop computer equipped with a 2014 Intel Core-I5 processor with 8Gbyte of RAM are 782 and 4606 seconds for the two meshes. This is to be compared with the computational cost of 35506 seconds reported in [4] to solve the same problem on a mesh with 49152 triangles (with an unspecified CPU). The difference in performance has to be attributed to the fact that the algorithm in [4] has a computational complexity that grows exponentially with the size of the triangulation, while our algorithm is affected by the classical polynomial computational complexity of FEM methods. Finally, we would like to note that the computational cost of our method is comparable if not better to the approach described in [9]. The use of implicit time-stepping in combination with Newton method as proposed in [41], which allows a drastic improvement in computational efficiency, is the next step in our future studies.

## 6 Conclusions

We presented a new result showing the one-to-one correspondence between the cut locus of a point  $p$  in a Riemannian manifold  $(M, g)$  and the zero set of the OTD  $\mu^*$  solution of the MK equations with  $f^+ = dV_g(M)\delta_p$  and  $f^- = dV_g$ . This new PDE-based characterization allows us to exploit standard finite element methods in combination with optimization techniques for the numerical approximation of the cut locus. Based on this result, we proposed a novel numerical approach for the identification of the cut locus of a point on 2d surfaces embedded in  $\mathbb{R}^3$  using the DMK method proposed in [20] for the solution of the of the MK equations. Numerical tests on few examples show that the cut locus can be efficiently identified with the developed strategy. The proposed DMK-based numerical approach can be easily extended to manifolds with dimension greater than two as long as the numerical solution of the PDE eq. (9a) is feasible.

## Acknowledgments

EF has been supported by the Centro di Ricerca Matematica “Ennio De Giorgi”. FF has been partially supported by MIUR-PRIN project 20178CJA2B *New frontiers of Celestial Mechanics: theory and applications*. MP has been partially supported by UniPD-SID-2016 project *Approximation and discretization of PDEs on Manifolds for Environmental Modeling*.

## References

- [1] Isaac Chavel. *Riemannian Geometry: A Modern Introduction*. Cambridge Studies in Advanced Mathematics. Cambridge University Press, 2 edition, 2006.
- [2] Carlo Mantegazza and Andrea Carlo Mennucci. Hamilton-Jacobi equations and distance functions on Riemannian manifolds. *Appl. Math. Optim.*, 47(1):1–25, January 2003.
- [3] Bernard Bonnard, Jean Baptiste Caillaud, Robert Sinclair, and Minoru Tanaka. Conjugate and cut loci of a two-sphere of revolution with application to optimal control. *Ann. Inst. H. Poincaré Anal. Non Linéaire*, 26(4):1081–1098, 2009.
- [4] Jin Ichi Itoh and Robert Sinclair. Thaw: A tool for approximating cut loci on a triangulation of a surface. *Experiment. Math.*, 13(3):309–325, 2004.
- [5] Marek Krzysztof Misztal, Jakob Andreas Bærentzen, Francois Anton, and Steen Markvorsen. Cut locus construction using deformable simplicial complexes. In *2011 Eighth International Symposium on Voronoi Diagrams in Science and Engineering (ISVD)*, pages 134–141. IEEE, June 2011.
- [6] Tamal K Dey and Kuiyu Li. Cut locus and topology from surface point data. In *Proceedings of the twenty-fifth annual symposium on Computational geometry*, pages 125–134, 2009.
- [7] Keenan Crane, C Weischedel, and M Wardetzky. Geodesics in heat: A new approach to computing distance based on heat flow. *ACM Trans. Graph.*, 2013.
- [8] François Générault, Edouard Oudet, and Bozhidar Velichkov. Cut locus on compact manifolds and uniform semiconcavity estimates for a variational inequality. arXiv preprint arXiv:2006.07222, 2020.
- [9] François Générault, Edouard Oudet, and Bozhidar Velichkov. Numerical computation of the cut locus via a variational approximation of the distance function. arXiv preprint arXiv:2006.08240, 2020.
- [10] Alessio Figalli and Cédric Villani. An approximation lemma about the cut locus, with applications in optimal transport theory. *Methods and Applications of Analysis*, 15(2):149–154, June 2008.
- [11] Alessio Figalli and Ludovic Rifford. Mass transportation on sub-riemannian manifolds. *Geom. Funct. Anal.*, 20(1):124–159, Jun 2010.
- [12] Alessio Figalli, Ludovic Rifford, and Cédric Villani. Tangent cut loci on surfaces. *Differ. Geom. Appl.*, 29(2):154–159, 2011.
- [13] Cédric Villani. Regularity of optimal transport and cut locus: From nonsmooth analysis to geometry to smooth analysis. *Discrete Contin. Dyn. Syst. Ser. A*, 30(2):559–571, January 2011.
- [14] Luigi Ambrosio. Lecture notes on optimal transport problems. In *Lecture Notes in Mathematics*, pages 1–52. Springer, Berlin, Heidelberg, 2003.
- [15] Cédric Villani. *Topics in optimal transportation*. Number 58 in Graduate studies in mathematics. American Mathematical Soc., 2003.
- [16] Cédric Villani. *Optimal Transport: Old and New*, volume 338. Springer Science & Business Media, 2008.
- [17] Filippo Santambrogio. *Optimal Transport for Applied Mathematicians*. Birkäuser, NY, 2015.
- [18] Aldo Pratelli. Equivalence between some definitions for the optimal mass transport problem and for the transport density on manifolds. *Ann. di Mat. Pura ed Appl.*, 184:215–238, 06 2005.
- [19] Lawrence C Evans and Wilfrid Gangbo. *Differential equations methods for the Monge–Kantorovich mass transfer problem*, volume 653. American Mathematical Soc., 1999.
- [20] Luca Berti, Enrico Facca, and Mario Putti. Numerical solution of the  $L^1$ -optimal transport problem on surfaces. ArXiv preprint available, 2021.
- [21] Enrico Facca, Sara Daneri, Franco Cardin, and Mario Putti. Numerical solution of monge–kantorovich equations via a dynamic formulation. *J. Scient. Comput.*, 82(3):1–26, 2020.
- [22] Enrico Facca, Franco Cardin, and Mario Putti. Towards a stationary Monge–Kantorovich dynamics: The physarum polycephalum experience. *SIAM J. Appl. Math.*, 78(2):651–676, 2018.
- [23] Takashi Sakai. *Riemannian geometry*, volume 149. American Mathematical Soc., 1996.
- [24] Jin Ichi Itoh and Minoru Tanaka. The Lipschitz continuity of the distance function to the cut locus. *Trans. Amer. Math. Soc.*, 353(1):21–40, 2001.
- [25] Bradford Fisher Kimball. Geodesics on a toroid. *Am. J. Math.*, 52(1):29–52, 1930.

- [26] Jens Gravesen, Steen Markvorsen, Robert Sinclair, and Minoru Tanaka. The cut locus of a torus of revolution. *Asian J. Math.*, 9(1):103–120, 03 2005.
- [27] Jürgen Jost. *Riemannian geometry and geometric analysis*, volume 42005. Springer, 2008.
- [28] L. E. Blumenson. A derivation of n-dimensional spherical coordinates. *Am. Math. Mon.*, 67(1):63–66, 1960.
- [29] Guy Bouchitté and Giuseppe Buttazzo. Characterization of optimal shapes and masses through Monge-Kantorovich equation. *J. Eur. Math. Soc.*, 3(2):139–168, 2001.
- [30] Mikhail Feldman and Robert J. McCann. Monge’s transport problem on a riemannian manifold. *Trans. Amer. Math. Soc.*, 354(4):1667–1697, 2001.
- [31] Mikhail Feldman and Robert J. McCann. Uniqueness and transport density in monge’s mass transportation problem. *Calc. Var. Partial Diff. Equ.*, 15(1):81–113, 2002.
- [32] Luigi De Pascale, Lawrence C Evans, and Aldo Pratelli. Integral estimates for transport densities. *Bull. London Mat. Soc.*, 36(3):383–395, 2004.
- [33] Filippo Santambrogio. Absolute continuity and summability of transport densities: simpler proofs and new estimates. *Calc. Var. Partial Diff. Equ.*, 36(3):343–354, 2009.
- [34] Gerhard Dziuk and Charles M Elliott. Finite element methods for surface pdes. *Acta Num.*, 22:289–396, 2013.
- [35] Jean-Marie Morvan. *Generalized Curvatures*, volume 2 of *Geometry and Computing*. Springer Science & Business Media, Berlin, Heidelberg, May 2008.
- [36] Anna-Karin Tornberg and Bjorn Engquist. Regularization techniques for numerical approximation of PDEs with singularities. *J. Scient. Comput.*, 19(1-3):527–552, December 2003.
- [37] Anna-Karin Tornberg and Bjorn Engquist. Numerical approximations of singular source terms in differential equations. *J. Comp. Phys.*, 200(2):462–488, November 2004.
- [38] Paolo Albano. On the stability of the cut locus. *Nonlinear Anal. Theory Methods Appl.*, 136:51 – 61, 2016.
- [39] Elena Bachini and Mario Putti. Geometrically intrinsic modeling of shallow water flows. *Math. Model. Num. Anal.*, 54(6):2125–2157, 2020.
- [40] Per-Olof Persson and Gilbert Strang. A simple mesh generator in Matlab. *SIAM Rev.*, 46(2):329–345, 2004.
- [41] Enrico Facca and Michele Benzi. Fast iterative solution of the optimal transport problem on graphs. *SIAM J. Sci. Comput.*, 2021. To appear, ArXiv preprint available.